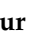*Article*

Effect of Dimpled Rib with Arc Pattern on Hydrothermal Characteristics of Al₂O₃-H₂O Nanofluid Flow in a Square Duct

Anil Kumar [1], Rajesh Maithani [1,*], Sachin Sharma [1], Sunil Kumar [2], Mohsen Sharifpur [3,4,*],
Tabish Alam [5], Naveen Kumar Gupta [6] and Sayed M. Eldin [7]

[1] Mechanical Engineering Department, UPES, Dehradun 248007, India
[2] Yogananda School of AI, Computers and Data Sciences, Shoolini University, Solan 173229, India
[3] Nanofluids Research Laboratory, Department of Mechanical and Aeronautical Engineering, University of
    Pretoria, Pretoria 0002, South Africa
[4] Department of Medical Research, China Medical University Hospital, China Medical University,
    Taichung 404, Taiwan
[5] CSIR-Central Building Research Institute, Roorkee 247667, India
[6] Mechanical Engineering Department, Institute of Engineering & Technology, GLA University,
    Mathura 281406, India
[7] Center of Research, Faculty of Engineering, Future University in Egypt, New Cairo 11835, Egypt
*   Correspondence: rmaithani@ddn.upes.ac.in (R.M.); mohsen.sharifpur@up.ac.za (M.S.)

Abstract: The present work is concerned with the experimental analysis of the thermal and hydraulic performance of $Al_2O_3 - H_2O$ nanofluid flow in dimpled rib with arc pattern in a square duct. The Alumina nanofluid consists of nanoparticles having a size of 30 nm. Reynolds number (Re_{num}) studied in the square duct range from 5000 to 26,000. The nanoparticle volume fraction (ϕ_{np}) ranges from 1.5% to 4.5%, the ratio of dimpled-arc-rib-height to print-diameter (H_{AD}/P_d) ranges from 0.533 to 1.133, the ratio of the dimpled-rib-pitch to rib height (P_{AD}/H_{AD}) range from 3.71 to 6.71 and dimpled arc angle (α_{AD}) range from 35° to 65°. The $Al_2O_3 - H_2O$-based nanofluid flow values of Nusselt number (Nu_{rs}) and friction factor (f_{rs}) are higher in comparison to pure water. The dimpled ribs in the arc pattern significantly improved the thermal-hydraulic performance of the investigated test section. The nanoparticle concentration of 4.5%, the ratio of dimpled arc rib height to print diameter of 0.933, the relative dimpled arc rib height of 4.64 and the dimpled arc angle of 55° deliver the maximum magnitude of the heat transfer rate. The maximum value of the thermal-hydraulic performance parameters was found to be 1.23 for $Al_2O_3 - H_2O$-based nanofluid flow in a dimpled rib with arc pattern square duct for the range of parameters investigated. Correlations of Nu_{rs}, f_{rs} and η_{rs} have been developed for the selected range of operating and geometric parameters.

Keywords: dimpled rib; rough surface; nanofluids; friction factor; turbulence

1. Introduction

Heat transfer (HT) is a thermal engineering subject that deals with thermal energy generation, transformation, and transfer [1]. Overall performance can be improved by using various methodologies and techniques, like either increasing the surface of the heat-transferring body or the heat transfer coefficient between the fluid and the surface that allows high heat transfer in a slight capacity [2]. Aside from the solicitation in heat transfer, hybrid nanofluids can also be blended for exceptional electrical, magnetic, chemical, and biological applications [3–8]. The great perspective of hybrid nanofluids for the augmentation of thermal energy in various applications leads to the development of effective and compact heat-transferring engineering equipment [9]. Ding et al. conducted several experiments to improve the thermal performance of heat transfer fluids and concluded that in many industrial sectors like power generation and chemical production, traditional heat transfer fluids play an important role. Naseema et al. [10] and Karthikeyan et al. [11] examined

the function of thermal conductivity of heat fluid transfer in the development of energy-efficient heat transfer equipment. Their analysis showed that the nonmetallic liquid thermal conductivity is much lesser as compared to the metallic liquids. Dormohammad et al. [12] and Shehzad et al. [13] have shown that natural convection and forced convection are two methods on the basis of which Nu and f can be classified, and that is necessary to improve the characteristics of HT so that the energy-saving efficiency in industries is increased. In the experiment, they used solid particles for heat transfer because they possess good conductivity characteristics. Tang et al. [14] investigated the possibility of increasing thermal conductivity by replacing the pure liquid with nanofluid, as nanofluids have better performance in comparison to pure water. Sharifpur et al. [15] and some others [16–19] concluded that under natural convection, the nanoparticle concentration is a significant factor in the enhancement of HT. Mansoury et al. [20] and Mayeli et al. [21] conducted a parametric investigation to assess HT increase in various heat exchangers containing $Al_2O_3 - H_2O$ nanofluid and found that by cumulative the solid volume fraction of the Al_2O_3 nanoparticles, the average heat transfer increases. Chun et al. [22] observed that a low particle concentration of nanofluids could boost heat conductivity by more than 20%; they also concluded that due to the high concentration of nanoparticles, there is an increase in the average Nu. Ghosh and Mukhopadhyay [23] observed that nanofluid thermo-physical properties are better as compared to conventional heat transfer fluids. Yang et al. [24] reported that as compared to alumina-zirconia/water nanofluid, alumina-water nanofluid has higher Nu and lower f.

Aliabadi and Hormozi [25] concluded that using $CuO - H_2O$ nanofluid instead of the base fluid, Nu, as well as f, are both plain and perforated channels have increased. When both heat transfer enhancement approaches discussed in this article are used simultaneously, a significant thermal performance factor of 1.34 is attained. Xuan and Li [26] measured the average Nu of $Al_2O_3 - H_2O$ nanofluid and reported 35% enhancement at 2 vol% of $Al_2O_3 - H_2O$ nanofluid. Their analysis showed that the f for the dilute nanofluids consisting of H_2O and Cu nanoparticles is approximately the same as that of H_2O. Xia et al. [27] investigated Al_2O_3 and TiO_2 nanofluids in a different microchannel for studying Nu and f. It is found that the performance of Al_2O_3 is better than TiO_2 for 1.0% of the volume fraction. Raei et al. [28] conducted a number of experiments on nanofluids and concluded that the thermal conductivity, as well as the heat transfer coefficient of the base fluid, can be enhanced by using porous metal. Ekiciler and Çetinkaya [29] analyzed the turbulent flow of water-based monotype nanofluid and hybrid nanofluid having a constant 1.0% nanoparticle volume fraction in a duct with rib. Heat transfer, pressure drop, temperature contour, and turbulence intensity were among the parameters studied and evaluated; they discovered that, while the increase in Nusselt number with monotype nanofluid is approximately 18.0%, the increase in Nusselt number with hybrid nanofluid is about 32.0%.

Pourpasha et al. [30] carried out optimization of the parameters affecting the HT coefficient of nanofluids (Al_2O_3/H_2O, CuO/H_2O, and Cu/H_2O). According to their findings, the optimized parameters increased Nu by 82% for Al_2O_3/H_2O nanofluids. Çobanoglu et al. [31] investigated the result of water-ethylene glycol mixture-based Fe_2O_3 nanofluids (0.01, 0.05, and 0.1 vol.%) on the annular flow propagation and heat transfer in the annuli of a double pipe heat exchanger at the low-pressure side of the refrigeration cycle; they noticed that the highest concentration has the most excellent transferred heat (13.6% increase in performance over the base fluid), the nanofluids with the most negligible concentration have the lowest pressure drop value (25% decrease over the working fluids), and the highest performance evaluation criteria with a tiny increase in exergy destruction (1.45% over the working fluids). Vinoth et al. [32] carried out an experiment with deionized water, Al_2O_3/H_2O nanofluid, and a hybrid nanofluid $Al_2O_3/CuO/H_2O$ at varying mass flow rates in a curved channel. Findings revealed that the rate of HT curved channel was improved by 11.98% compared to the straight channel. Additionally, the utilization of $Al_2O_3/CuO/H_2O$ hybrid nanofluid increased the rate of heat transfer by 3.5% and 2.1%, respectively, in comparison to water and Al_2O_3/H_2O nanofluid. Fujimoto et al. [33] ex-

amined the turbulent *HT* capability of graphene nanofluids in a horizontal circular tube experimentally and numerically. According to their findings, the *Nu* of graphene nanofluid had an increase of 33% compared to water. Ho et al. [34] experimentally investigated the laminar and forced convection heat transfer by using Al_2O_3/PCM nanofluids in a concentric double-tube duct. Heat transfer, pressure drop, thermal and hydraulic performance, and flow parameters were all analyzed and evaluated. According to their findings, a high total flow rate combined with a high concurrent flow ratio can effectively increase heat transfer efficacy. Jalili et al. [35] studied *HT* convection in a countercurrent double-tube heat exchanger with varied fins and Al_2O_3/H_2O and TiO_2/H_2O nanofluids (0.4%, 2%, 4%, 6%). Results revealed that Al_2O_3/H_2O nanofluid has a more excellent convection *HT* coefficient than TiO_2/H_2O and H_2O. In addition, increasing nanofluid concentration from 0.4% to 6% increased convection *HT* by 12%. Huihui Zhang et al. [36] experimentally investigated the pressure-drop, and nanoparticle deposition physiognomies of multiple twisted tapes with partitions in turbulent duct fluid flows using air as working fluid. Penetration tests for nano-sized particles and pressure loss measurements were carried out in the empty duct, and the construction process was fitted with twisted tapes and zones operating at the same pumping power; they revealed that the penetration efficiency of nanoparticles enhanced with nanomaterials diameter and mass flow rate. Omri et al. [37] investigated a novel heat exchanger configuration using CNT-nanofluid and jet impingement with a uniform wall temperature profile. The volume fraction of the selected nanoparticles ranges from 0 to 5%, along with the varying fin's height. It was concluded that the use of CNT nanofluid significantly enhances the heat transfer rate.

From the literature review, no research has been carried out on square duct heat exchangers using dimpled ribs with arc patterns of roughness on the heat-transferring surface. Thus, utilizing nanofluid and dimpled rib with arc pattern turbulence promotor can significantly improve the thermal performance of the heat exchanger. Hence, the present study aims to analyze the heat transfer experimentally, and friction factor characteristics of a ribbed square duct having a dimpled rib with an arc pattern on the heated wall roughened duct with $Al_2O_3 - H_2O$ nanofluid flow. This research fills the lack of experimental research for $Al_2O_3 - H_2O$ nanofluid flow in a ribbed square duct with dimpled rib with arc pattern.

The primary goals of the current experimental analysis are:

- To investigate the effect of arc rib pitch, arc flow attack angle, dimpled arc rib, and volume fraction on *Nu* and *f* with $Al_2O_3 - H_2O$ nanofluid flow in a ribbed square duct.
- To determine the prolific dimpled rib with arc pattern and flow parameters for $Al_2O_3 - H_2O$ nanofluid flow in a ribbed square duct by considering the thermal-hydraulic performance.

2. Rib Parameters

The measurements can describe the rib roughness of arc rib height (H_{AD}), the Print diameter of arc rib (P_d) and the pitch between arcs (P_{AD}). Dimensionless roughness parameters have been used to express these parameters, viz., relative arc rib height (H_{AD}/P_d), relative rib pitch (P_{AD}/H_{AD}) and arc angle (α_{AD}). Figure 1 represents the geometry of the dimpled rib arc pattern. Table 1 demonstrates the ranges of dimpled arc rib and flow parameters that are selected in the present investigation for enhancing the thermal performance of the duct.

Table 1. Range of dimpled arc rib and flow parameters.

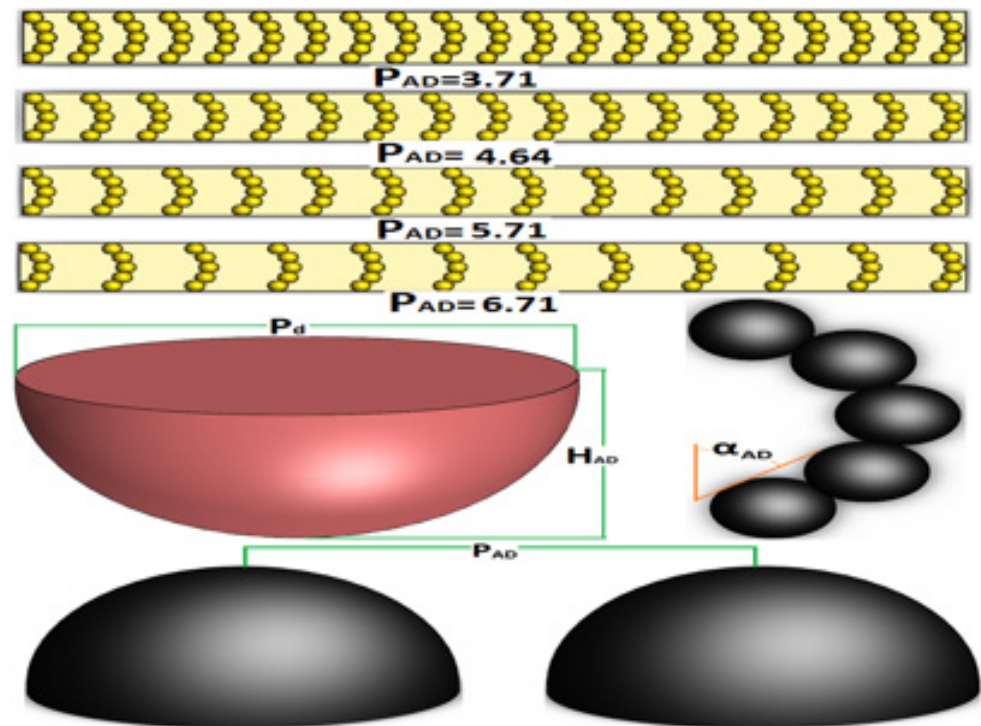| S.N.	Parameters	Ranges
1.	H_{AD}/P_d	0.533–1.133
2.	P_{AD}/H_{AD}	3.71–6.71
3.	α_{AD}	35°–65°
4.	ϕ_{np}	1.5–4.5%
5.	d_{np}	30 nm
6.	Re_{num}	5000–26,000

Figure 1. Discuss arc with dimpled rib parameters.

3. Experimental Setup

The components of the experimental setup are designed following the ASHRAE standards [38], which are discussed in this section, and the experimental test rig is shown in Figure 2. A submersible pump is employed for circulating the fluid through the test section integrated with a flow meter with a changeable area for measurement and controlling the fluid flow in the loop and the test division. The pressure drop during fluid circulation was measured with a differential pressure manometer connected at the inlet and outlet of the test section. The heat was supplied to the test section with an electric heater built of nichrome wire wrapped around a mica sheet. The auto-transformer was incorporated to manage the power supply, and the magnitude of current and voltage were determined by a multi-meter. The temperature of the examination unit was measured at various locations with the help of calibrated T-type thermocouples, and a digital micro voltmeter (DVM) was utilized to display the temperature. The drop in the pressure across the test section during experimentation was recorded by a digital micro-manometer having the least count of 1 Pa. A number of experiments were performed for varying geometric parameter sets of dimpled arcs rib roughness on the heated surface at different flow rates of fluid in the duct to accumulate the experimental data viz. plate temperature, inlet and outlet temperature of nanofluids and pressure drop across the channel test section. All measurements were made under steady-state circumstances. Further, the data reduction has been performed by utilizing the raw data to obtain the heat flow and friction in dimensionless form as a purpose of a system and operating parameters. A condenser is installed after the test section to bring down the temperature of the nanofluid at the ambient level as the nanofluid is circulated in the closed loop.
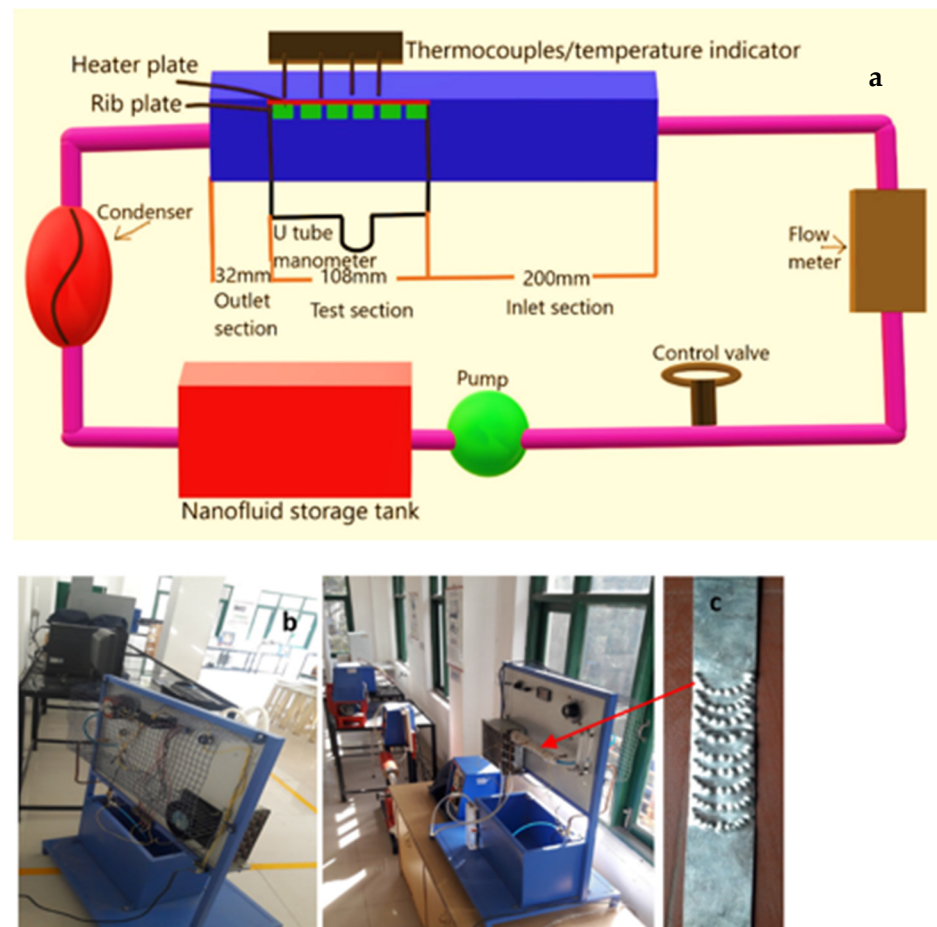
Figure 2. (**a**) Schematic and (**b**) pictorial view of the experimental setup and (**c**) dimpled surface.

4. Nanofluid Preparation and Its Thermo-Physical Properties

The $Al_2O_3 - H_2O$ nanofluid has been prepared for four different volume concentrations of 1.5%, 2.5%, 3.5% and 4.5% by mixing the Al_2O_3 nanoparticles of 99.9% purity in distilled water. As a surfactant, sodium dodecyl benzene sulphonate was utilized to make Al_2O_3/H_2O more soluble and stable nanofluid with a surfactant to nanofluid proportions of 10:1. Sodium dodecyl benzene sulphonate is a high-content anionic surfactant having good emulsility and dispersity properties as compared to other surfactants. The significance pH for improving the stability of Al_2O_3-based nanofluid was attained at 5.0. Better dispersing of nanoparticles in distilled water is required to obtain a homogeneous fluid. The homogenization and sonication of all solutions were carried out in an ultrasonic homogenizer, shown in Figure 3, for three days to reduce particle aggregation and nanofluid sedimentation. The stability of the nanofluid is checked by using a UV-vis spectrometer (Evolution 201). To check the visual stability of nanofluid, Figure 3 shows the photograph of nanofluid taken immediately after preparation as well as after two and then after four days of nanofluid preparation.

Nanoparticles and base fluid properties are used to calculate the thermo-physical parameters of nanofluids. The nanofluid density is calculated using the following relationship [39]

$$\rho_{nf} = (1 - \varphi)\rho_{bf} + \varphi\rho_{np} \tag{1}$$

To compute the nanofluid's specific heat following equation is obtained [39]:

$$\left(\rho C_p\right)_{nf} = (1 - \varphi)\left(\rho C_p\right)_{bf} + \varphi\left(\rho C_p\right)_{np} \tag{2}$$
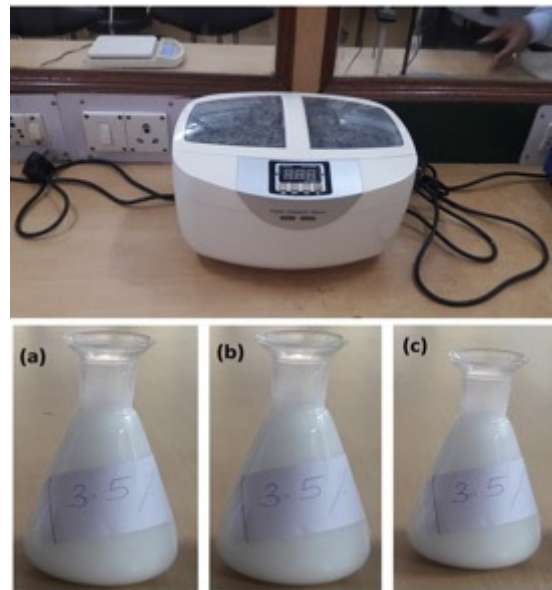
Figure 3. Pictorial view of the homogenizer and stability of Al_2O_3 nanofluid (**a**) Immediately after preparation (**b**) After 2 days (**c**) After 4 days.

The following correlations are used to affect the nanofluid's thermal conductivity [40,41]:

$$k_{eff} = k_{static} + k_{Brownian}$$

$$k_{static} = k_{bf} \left[\frac{\left(k_{np} + 2k_{bf}\right) - 2\varphi\left(k_{bf} - k_{np}\right)}{\left(k_{np} + 2k_{bf}\right) + \varphi\left(k_{bf} - k_{np}\right)} \right] \tag{3}$$

$$k_{Brownian} = 5 \times 10^4 \beta \varphi \rho_{bf} C_{p,bf} \sqrt{\frac{KT}{2\rho_{np}R_{np}}} f(T, \varphi) \tag{4}$$

where $K(Boltzmann\ constant) = 1.3807 \times 10^{-23}$ J/K, T is the temperature, and β is the portion of the liquid volume that travels with particles. The value of $\beta = 8.4407(100\varphi)^{-1.07304}$ for Al_2O_3 particles.

Modeling,

$$f(T, \varphi) = \left(2.8217 \times 10^{-2}\varphi + 3.917 \times 10^{-3}\right)\left(\frac{T}{T_o}\right) + \left(-3.0669 \times 10^{-2}\varphi - 3.91123 \times 10^{-3}\right) \tag{5}$$

For $1\% \leq \varphi \leq 4\%$ and $300\ \text{K} < T < 325\ \text{K}$, $T_0 = 293$ K.

The following empirical relation is used to calculate dynamic viscosity [42]:

$$\mu_{eff} = \mu_{bf} \times \frac{1}{\left(1 - 34.87(d_{np}/d_f)^{-0.3} \times \varphi^{1.03}\right)} \tag{6}$$

$$d_f = \left[\frac{6M}{N\pi\rho_{bf}}\right]^{1/3} \tag{7}$$

where M is the base fluid's molecular weight, $N = 6.022 \times 10^{23}\ \text{mol}^{-1}$ is the Avogadro number, and ρ_{bf} is the base fluid's mass density at $T_0 = 293$ K.

5. Validation of Experimental Setup

The obtained experimental results were compared with the literature data in terms of Nu_{ss} and f_{ss} in the situation of a smooth surface square channel, as shown in Figure 4a,b.

The values of Nu_{ss} and f_{ss} of a smooth surface square duct under each Re_{num} value are compared with available standard correlation results under similar experimental conditions.
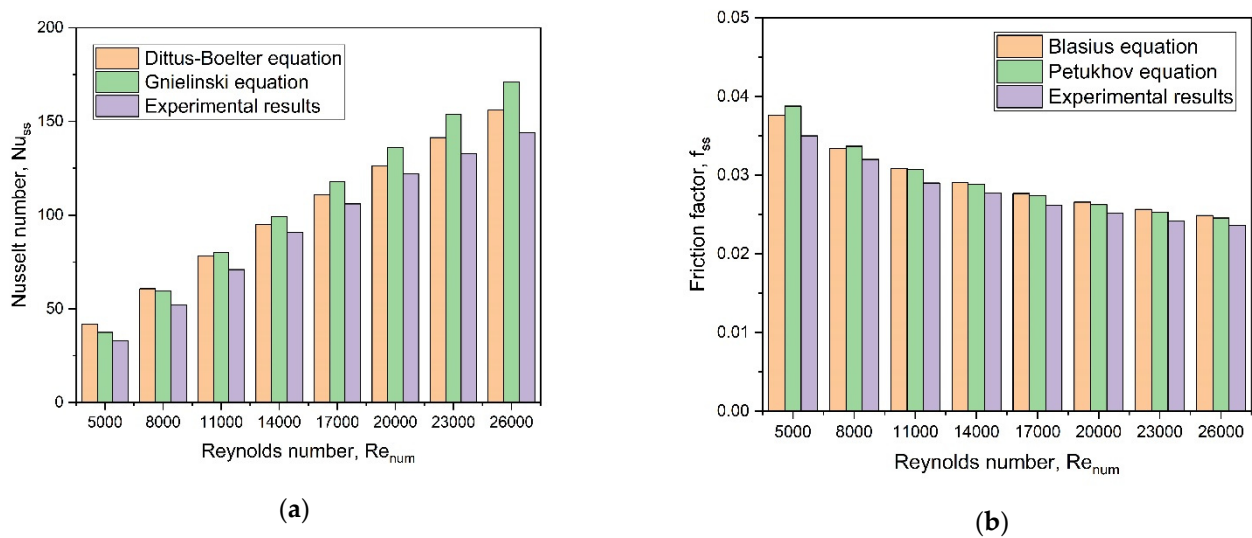

Figure 4. Validation of experimental results for a smooth surface duct with (**a**) Nu_{ss} (**b**) f_{ss}.

Dittus–Boelter equation [43] (Equation (8)) and Gnielinski equation [44] (Equation (9)) of Nu_{ss} for the smooth surface wall are given as:

$$Nu_{ss} = 0.023Re_{num}^{0.8}Pr_{num}^{0.4} \tag{8}$$

$$Nu_{ss} = \frac{(f_{ss}/8)(Re_{num} - 1000)Pr_{num}}{1 + 12.7(f_{ss}/8)^{1/2}(Pr_{num}^{2/3} - 1)} \ for \ 3000 < Re_{num} < 10{,}000 \tag{9}$$

Blasius equation [44] and Petukhov equation [44] of f_{ss} for the smooth surface wall are given as:

$$f_{ss} = 0.316Re_{num}^{-0.25} \tag{10}$$

$$f_{ss} = (0.79lnRe_{num} - 1.64)^{-2} \tag{11}$$

The result of these comparisons is shown in Figure 4a,b. The figure indicates that there was extremely strong agreement between the current analysis conclusions and those predicted by the Dittus–Boelter equation and Gnielinski equation of, Nu_{ss} and Blasius equation, and Petukhov equation of f_{ss} for a smooth surface.

Figure 4a,b clearly illustrated that the average deviation of Nu_{ss} and f_{ss} was approximately 3.37% and 3.09%, respectively, which is an acceptable range.

6. Data Reduction

The calculation procedure of Re_{num}, Nu_{rs}, f_{rs} and η_{per} are presented in the present section. The data reduction is carried out by fetching the experimental data at the steady state condition and using the energy balance equation. The data in the form of temperature and pressure drop across the test channel is reduced in the non-dimensional form of the Nusselt number and the friction factor. The heater power supply is calculated by the equation [42].

$$Q_{in} = I \times V \tag{12}$$

The energy absorbed by the fluid in the duct is computed using the formula

$$Q_{out} = \dot{m}c_p(T_o - T_i) \tag{13}$$

The h between the fluid and the heated surface is calculated as

$$h = \frac{Q_{out}}{A_p\left(T_{pw} - T_f\right)}$$ (14)

The value of Re_{num} is determined by

$$Re_{num} = \frac{\rho_{nf} u_m D_h}{\mu_{nf}}$$ (15)

The equation to determine the Nu_{rs} is

$$Nu_{rs} = \frac{h\, D_h}{k_{nf}}$$ (16)

and the f_{rs} is calculated from

$$f_{rs} = \frac{2D_h \Delta p_d}{\rho_{nf} L u_m^2}$$ (17)

7. Uncertainty Analysis

The uncertainty of dimensionless numbers, such as Nu_{rs} and f_{rs}, was calculated with the method proposed by Kline [45]. The uncertainty in a measurement of "y" when the major experimental parameters are computed by using specific measured quantities:

$$\frac{\delta y}{y}\frac{\delta y}{y} = \left[\left(\frac{\delta y}{\delta x_1}\delta x_1\right)^2 + \left(\frac{\delta y}{\delta x_2}\delta x_2\right)^2 + \left(\frac{\delta y}{\delta x_3}\delta x_3\right)^2 + \cdots + \left(\frac{\delta y}{\delta x_n}\delta x_n\right)^2\right]^{0.5}$$ (18)

where, $\delta x_1, \delta x_2, \delta x_3, \ldots \delta x_n$ are the possible error in the measurement of $x_1, x_2, x_3, \ldots x_n$.

δ_y is absolute uncertainty, and $\frac{\delta_y}{y}$ the relative uncertainty. The main uncertainty analysis equations are given below:

A.　Uncertainty in Nu_{rs}

$$\frac{\delta Nu_{rs}}{Nu_{rs}} = \left[\left(\frac{\delta D_h}{D_h}\right)^2 + \left(\frac{\delta h_t}{h_t}\right)^2 + \left(\frac{\delta k_{nf}}{k_{nf}}\right)^2\right]^{0.5}$$ (19)

B.　Uncertainty in f_{rs}

$$\frac{\delta f_{rs}}{f_{rs}} = \left[\left(\frac{\delta D_h}{D_h}\right)^2 + \left(\frac{\delta u_m}{u_m}\right)^2 + \left(\frac{\delta L_t}{L_t}\right)^2 + \left(\frac{\delta \rho_{nf}}{\rho_{nf}}\right)^2 + \left(\frac{\delta \Delta p}{\Delta p}\right)^2\right]^{0.5}$$ (20)

The uncertainty for key parameters determined, Nu_{rs} and f_{rs} of the existing experimental examination is found to be $\pm 4.41\%$ and $\pm 5.95\%$, respectively. To show the variation of Nu_{rs} and f_{rs} as a function of Re_{num}, the error bars are shown in Figure 5a,b, respectively.
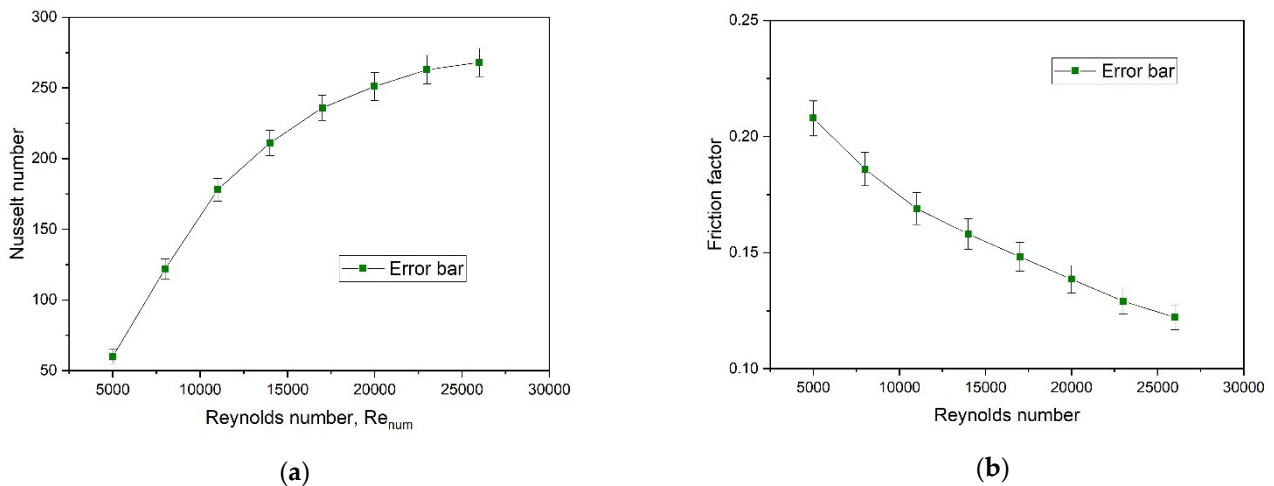
(**a**)

(**b**)

Figure 5. Error bars (**a**) Nusselt number (**b**) friction factor.

8. Results and Discussion

Experimental results are reported in terms of Nu_{rs}, f_{rs} and η_{per} as a function of Re_{num}, ranging from 5000 to 26,000, ϕ_{np} from 1.5% to 4.5% at constant d_{np} of 30 nm, H_{AD}/P_d from 0.533 to 1.133, P_{AD}/H_{AD} from 3.71 to 6.71 and α_{AD} range from 35° to 65°. The effects of nanoparticle volume fraction variation and artificially rib-roughened square duct on heat transfer are studied. Figure 6 shows the variation of Nu_{rs} and f_{rs} with Re_{num} at different ϕ_{np} of Al_2O_3 nanoparticle ranging from 1.5% to 4.5% of the entire test surface with the rib-roughened wall, which is performed at d_{np} of 30 nm, $H_{AD}/P_d = 0.933$, $P_{AD}/H_{AD} = 4.64$, and $\alpha_{AD} = 55°$. Figure 6a illustrates that as Re_{num} increased, Nu_{rs} also increased, and it also shows an enhancement in average heat transfer by 2.06%, 7.02% and 10.74% at $\phi_{np} = 2.5\%$, 3.5% and 4.5%, respectively, when compared to $\phi_{np} = 1.5\%$. This enhancement is due to the nanofluid's thermal conductivity and Brownian motion increment. Whereas Figure 6b illustrates that f_{rs} decreased as Re_{num} increased, and when the concentration of nanoparticles increased average friction factor increased. Furthermore, the friction factor is augmented around 5.55%, 9.25% and 13.15% at $\phi_{np} = 2.5\%$, 3.5% and 4.5%, respectively, in comparison to $\phi_{np} = 1.5\%$.
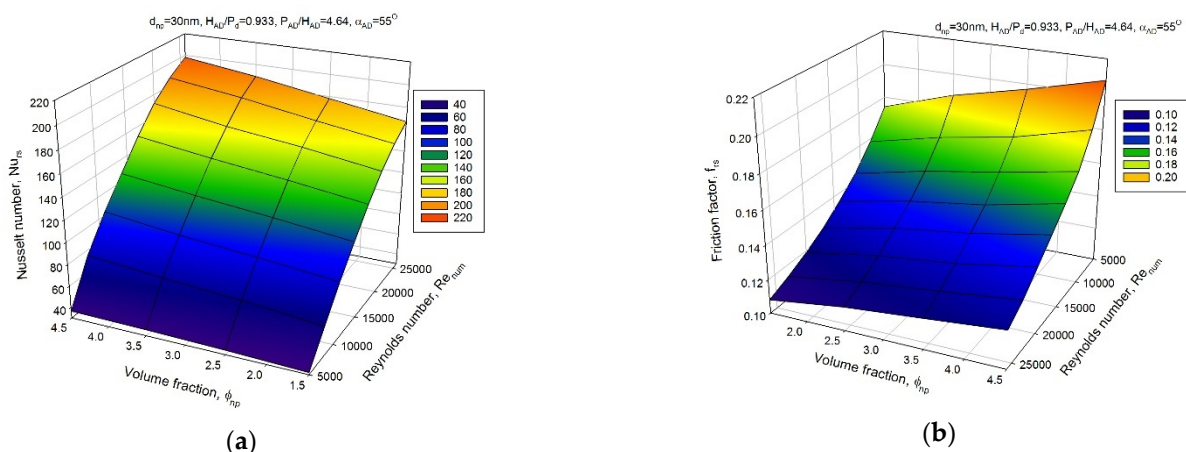

(**a**)

(**b**)

Figure 6. (**a**) Variation of Nu_{rs} with ϕ_{np} and Re_{num} (**b**) Variation of f_{rs} with ϕ_{rs} and Re_{num}.

The maximum heat transfer rate and flow friction are observed at $\phi_{np} = 4.5\%$ for all values of Re_{num}. Figure 7 shows the variation of Nu_{rs} and f_{rs} with Re_{num} at H_{AD}/P_d ranging from 0.533 to 1.133 executed at fixed parameters d_{np} of 30 nm, $\phi_{np} = 4.5\%$, $P_{AD}/H_{AD} = 4.64$, and $\alpha_{AD} = 55°$. Figure 7a shows an enhancement in average heat transfer of 7.69%, 14.52% and 29.9% at $H_{AD}/P_d = 0.733$, 0.933 and 1.133, respectively when compared to $H_{AD}/P_d = 0.533$.

The general trends of heat transfer enhancement for the different values of relative arc rib height first immediately increased for $H_{AD}/P_d = 0.533$ to 0.933 and then decreased for $H_{AD}/P_d = 1.133$ for all values of Re_{num} due to the effect of stronger rotational momentum of secondary flow along the ribs, it may line the main flow to speed up it, providing a more heat transfer. The maximum heat transfer enhancement is found at $H_{AD}/P_d = 0.933$. Whereas Figure 7b demonstrated that f_{rs} decreases as Re_{num} increased as well as it is minimum at $H_{AD}/P_d = 0.533$ and maximum at $H_{AD}/P_d = 1.133$ for all values of Re_{num}. From the same figure, it is also concluded that the friction factor is augmented around 9.98%, 21.95% and 33.03% at $\frac{H_{AD}}{P_d} = 0.733$, 0.933 and 1.133, respectively, in comparison to $H_{AD}/P_d = 0.533$.
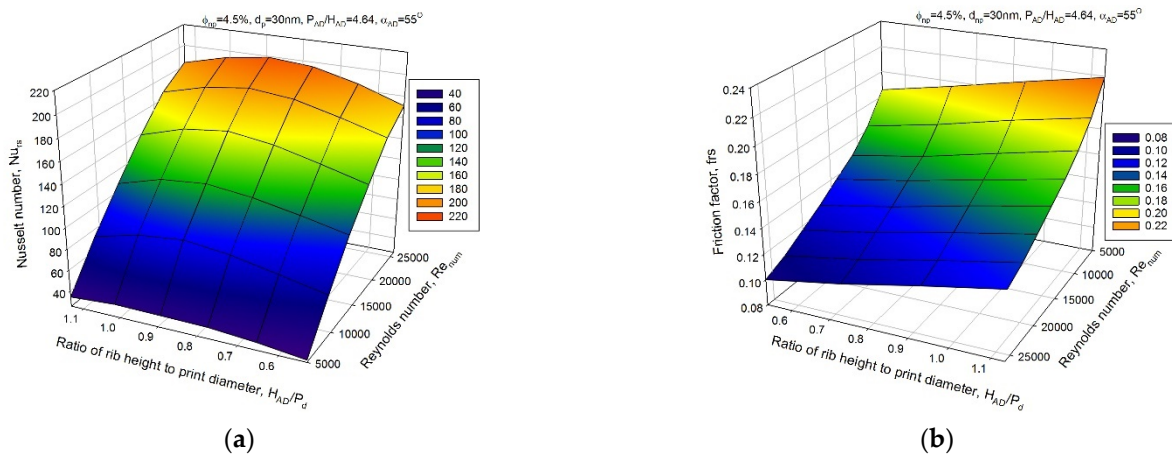

(a)

(b)

Figure 7. (**a**) Variation of Nu_{rs} with H_{AD}/P_d and Re_{num} (**b**) Variation of f_{rs} with H_{AD}/P_d and Re_{num}.

The effect of P_{AD}/H_{AD} on Nu_{rs} and f_{rs} with Re_{num} is illustrated in Figure 8, where P_{AD}/H_{AD} ranging from 3.71 to 6.71 and other parameters, d_{np} =30 nm, ϕ_{np} = 4.5%, $H_{AD}/P_d = 0.933$ and α_{AD} =55° were fixed. Figure 8a clearly indicates that Nu_{rs} increased as Re_{num} increased, and it is maximum when P_{AD}/H_{AD} =4.64, minimum at $P_{AD}/H_{AD} = 6.71$. Figure 8a also indicated an enhancement of 5.32%, 9.83% and 2.87% in average heat transfer at $P_{AD}/H_{AD} = 3.71$, 4.64 and 5.71, respectively, as compared to $P_{AD}/H_{AD} = 6.71$. The heat transfer coefficient raised when the value of relative rib pitch increased from 3.71 to 4.64, and then it decreased with a further increase in the value of relative rib pitch for all values of Re_{num}. Figure 8b clearly confirms that f_{rs} is minimum at $P_{AD}/H_{AD} = 6.71$ and maximum at $P_{AD}/H_{AD} = 3.71$. It is also witnessed that friction factor is improved around 32.34%, 20.51% and 10.25% at $P_{AD}/H_{AD} = 3.71$, 4.64 and 5.71, respectively, concerning $P_{AD}/H_{AD} = 6.71$. The details of fluid flow for the cases of arc angle and arc-shaped ribs are shown in Figure 9. It displayed the variation of Nu_{rs} and f_{rs} with Re_{num} at α_{AD} ranging from 35° to 65° when other operating parameters are kept constant as d_{np} of 30 nm, ϕ_{np} = 4.5%, $H_{AD}/P_d = 0.933$ and $P_{AD}/H_{AD} = 4.64$.

Figure 9a shows an enhancement in average heat transfer of 8.43%, 13.08% and 4.64% at α_{AD} =45°, 55° and 65° respectively, when compared to α_{AD} =35°. It is also observed that the heat transfer coefficient enhanced when the arc angle increased from 35° to 55°, and then it decreased with a further increase in arc angle. Moreover, a higher heat transfer rate is found at $\alpha_{AD} = 55°$ due to the strong secondary flow-induced arc angle of dimpled ribs inside the flow channel, and α_{AD} =35° provides the low heat transfer rate for all values of Re_{num}. Figure 9b indicates that f_{rs} increases when the arc angle increases from 35° to 55°, and then it decreases with a further increase in arc angle. An enhancement of 22.46%, 34.58% and 10.35% is found in friction factor at $\alpha_{AD} = 45°$, 55° and 65° respectively, when compared to $\alpha_{AD} = 35°$. Furthermore, from all these cases investigated, it is observed that the maximum heat transfer rate is found at $\phi_{np} = 4.5\%$, $H_{AD}/P_d = 0.933$, $P_{AD}/H_{AD} = 4.64$ and $\alpha_{AD} = 55°$ for all values of Re_{num}. The results reveal a stronger rotational momentum of secondary flow along the dimpled arc pattern ribs shown in Figure 10. It is seen from the flow pattern that the main flow is guided over the dimpled rib with an arc pattern, which tends to increase the turbulence intensity. On the other side, the secondary flow is developed in the vicinity of the dimpled rib,

which tends to boost the intensity of turbulence of the fluid, thus enhancing the rate of heat transfer. Furthermore, it is evident from this discussion that the ratio of rib height to print, the ratio of rib pitch to rib height, and the arc angle should be maintained to increase the velocity of the fluid moving through the duct to induce local turbulence.
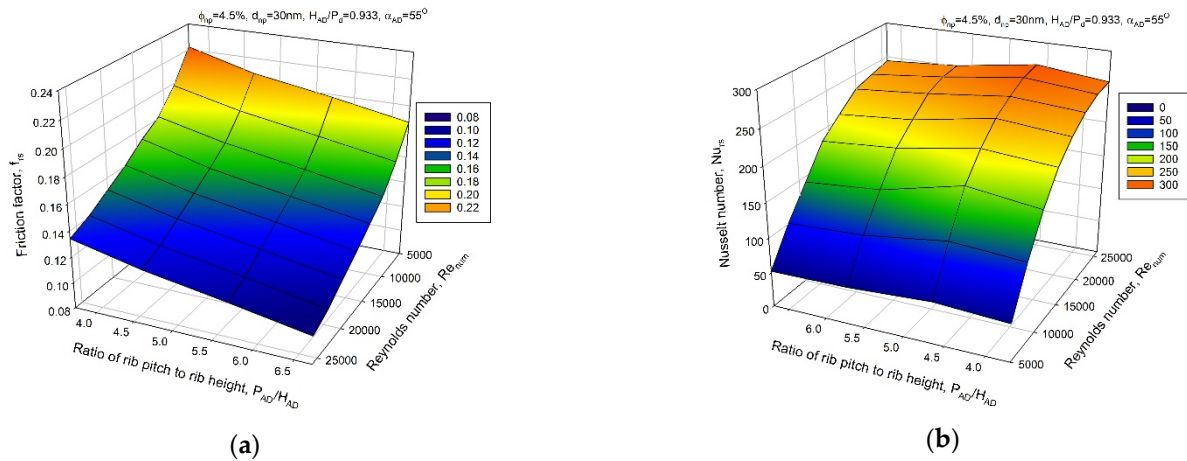

Figure 8. (**a**) Variation of Nu_{rs} with P_{AD}/H_{AD} and Re_{num} (**b**) Variation of f_{rs} with P_{AD}/H_{AD} and Re_{num}.
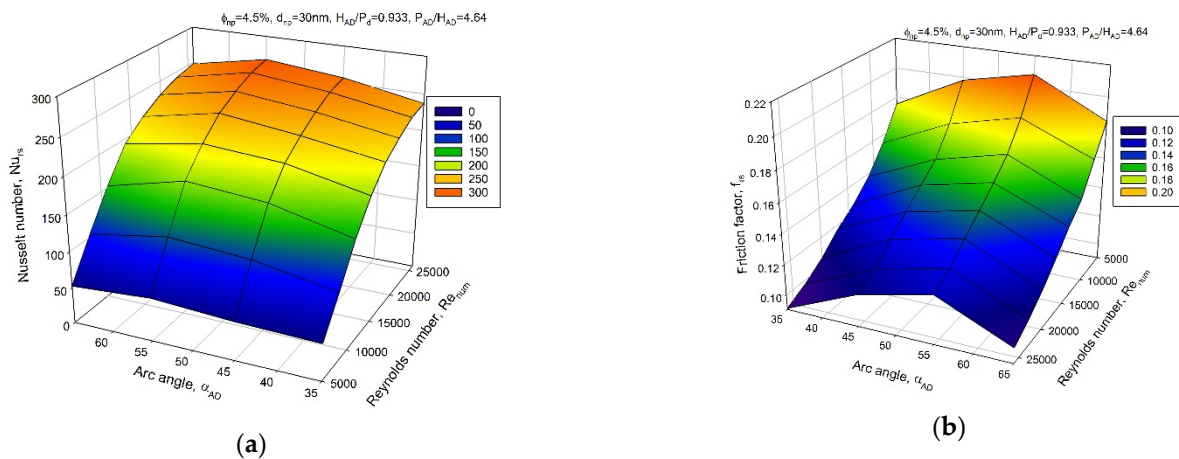

Figure 9. (**a**) Variation of Nu_{rs} with α_{AD} and Re_{num} (**b**) Variation of f_{rs} with α_{AD} and Re_{num}.

The thermal-hydraulic performance (η_{per}) of three different dimpled with combined arc-shaped ribbed square ducts is described in Figure 11. The thermal-hydraulic performance was expressed as $\eta_{per} = \frac{Nu_{rs}}{Nu_{ss}} / \left(\frac{f_{rs}}{f_{ss}}\right)^{1/3}$ [46]. The greater the value of this parameter, the better the performance of the heat exchanger. Figure 11a shows the effect of the ratio of rib height to print (H_{AD}/P_d) range from 0.533 to 1.133 on thermal hydraulic performance for selected values of Re_{num}, where it can be experiential that the value of η_{per} is increased when the value of H_{AD}/P_d increases from 0.533 to 0.933, and then it decreases with a further increase in the value of H_{AD}/P_d. It is evident from this figure that there is an enhancement of 2.02%, 13.84% and 19.79% in overall thermal performance at $H_{AD}/P_d = 0.533$, 0.733 and 0.933, respectively, when compared to $H_{AD}/P_d = 1.133$ and maximum value of η_{per} is found at $H_{AD}/P_d = 0.933$ for $Re_{num} = 11,000$. Figure 11b represents the thermal-hydraulic performance as a function of the ratio of rib pitch to rib height (P_{AD}/H_{AD}), ranging from 3.71 to 6.71 for the particular values of Re_{num}. From the figure, it can be clearly seen that the value of η_{per} is increases when the value of P_{AD}/H_{AD} increases from 3.71 to 4.64 and then it starts decreasing with a further increase in the value of P_{AD}/H_{AD} from 4.64 to 1.133. There is an enhancement of 8.73%, 20.03% and 3.98% in overall thermal performance at

$P_{AD}/H_{AD} = 3.71$, 4.64 and 5.71, respectively, with respect to $P_{AD}/H_{AD} = 6.71$. The highest value of the thermal-hydraulic performance is observed at $P_{AD}/H_{AD} = 4.64$ and lowest at $P_{AD}/H_{AD} = 6.71$ for $Re_{num} = 11,000$. Figure 11c represents the thermal-hydraulic performance as a function of arc angle in dimpled rib (α_{AD}) equal to $35°$, $45°$, $55°$ and $65°$ for the particular values of Re_{num}. Here it can be clearly recognized that the value of η_{per} is increases when the value of α_{AD} increases from $35°$ to $55°$ and then it starts decreasing with a further increase in the value of α_{AD}. The thermal-hydraulic performance is significantly high, about 13.01%, 16.36% and 3.85%at $\alpha_{AD} = 45°$, $55°$ and $65°$ respectively, when compared to $\alpha_{AD} = 35°$. The highest value of the thermal-hydraulic performance is observed at $\alpha_{AD} = 55°$ and lowest at $\alpha_{AD} = 35°$ for $Re_{num} = 11,000$.
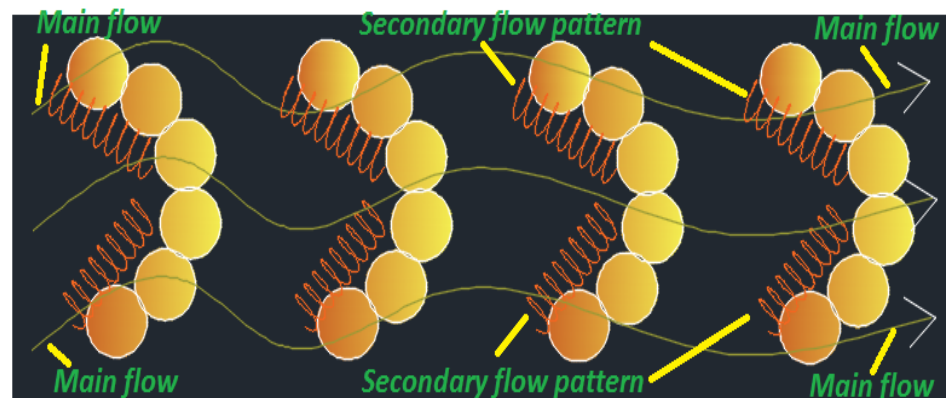
Figure 10. Secondary flow pattern in dimpled-arc ribs.
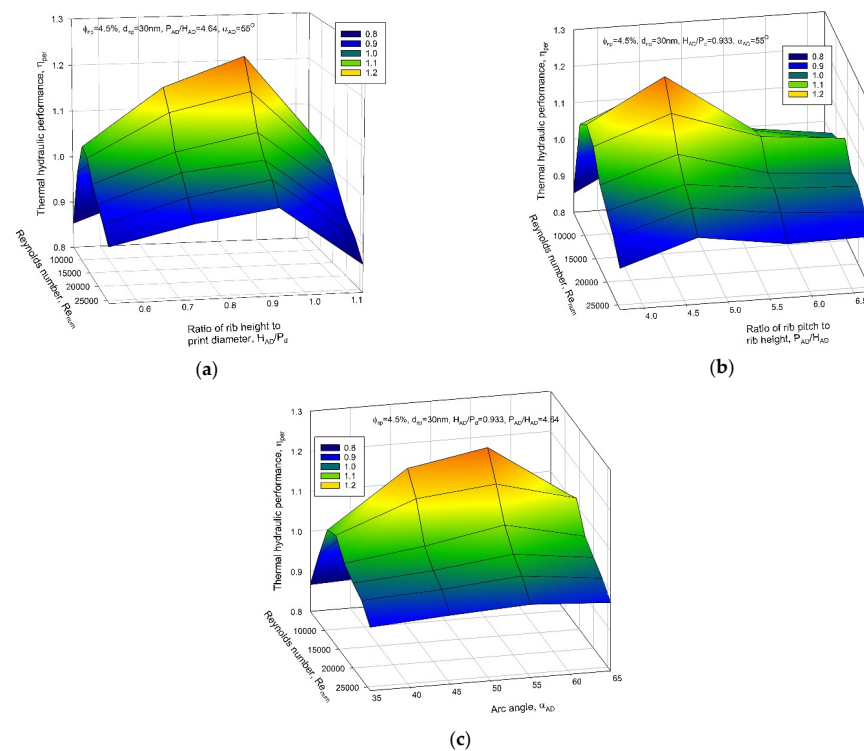
Figure 11. (**a**) Variation of η_{per} with H_{AD}/P_d and Re_{num} (**b**) Variation of η_{per} with P_{AD}/H_{AD} and Re_{num} (**c**) Variation of η_{per} with α_{AD} and Re_{num}.

9. Correlations for Nusselt Number and Friction Factor

The discussion of results reveals that the selected parameters for investigation are a strong function in determining the Nu_{rs}, f_{rs} and η_{rs} values. The yielded experimental

data of Nu_{rs}, f_{rs} and η_{rs} is utilized in the development of the correlations that will be valid for the selected range of Re. The functional relationship for Nu_{rs}, f_{rs} and η_{rs} for selected operating and geometric parameters is given as:

$$Nu_{rs} = f\left(Re, \phi_{np}, H_{AD}/P_d, P_{AD}/H_{AD}, \alpha_{AD}\right) \tag{21}$$

$$f_{rs} = f\left(Re, \phi_{np}, H_{AD}/P_d, P_{AD}/H_{AD}, \alpha_{AD}\right) \tag{22}$$

$$\eta_{rs} = f\left(Re, H_{AD}/P_d, P_{AD}/H_{AD}, \alpha_{AD}\right) \tag{23}$$

The experimental values are subjected to regression analysis in order to determine statistical correlations between Nu_{rs}, f_{rs} and η_{rs} for the selected geometrical and flow parameters.

The values result in the following correlation for Nu_{rs}.

$$Nu_{rs} = 0.019 \times Re^{0.91} \, \phi_{np}^{0.07} \, (H_{AD}/P_d)^{0.011} (P_{AD}/H_{AD})^{-0.17} (\alpha_{AD})^{0.14} \tag{24}$$

Likewise, a statistical correlation for f_{TT} and η_{TT} can be written as

$$f_{rs} = 1.56 \times Re^{-0.33} \, \phi_{np}^{0.11} \left(\frac{H_{AD}}{P_d}\right)^{0.25} \left(\frac{P_{AD}}{H_{AD}}\right)^{-0.33} (\alpha_{AD})^{0.3} \tag{25}$$

$$\eta_{rs} = 0.85 \times Re^{0.015} \left(\frac{H_{AD}}{P_d}\right)^{0.002} \left(\frac{P_{AD}}{H_{AD}}\right)^{-0.05} (\alpha_{AD})^{0.029} \tag{26}$$

In order to determine the variation between the experimental and predicted data of Nu_{rs}, f_{rs} and η_{rs}, a comparative analysis is carried out, and the outcome is represented in are presented in Figure 12a–c. The difference of experimental and predicted data of Nu_{rs}, f_{rs} and η_{rs} has an average deviation of $\pm 10.2\%$, $\pm 9\%$ and $\pm 9.3\%$, respectively.
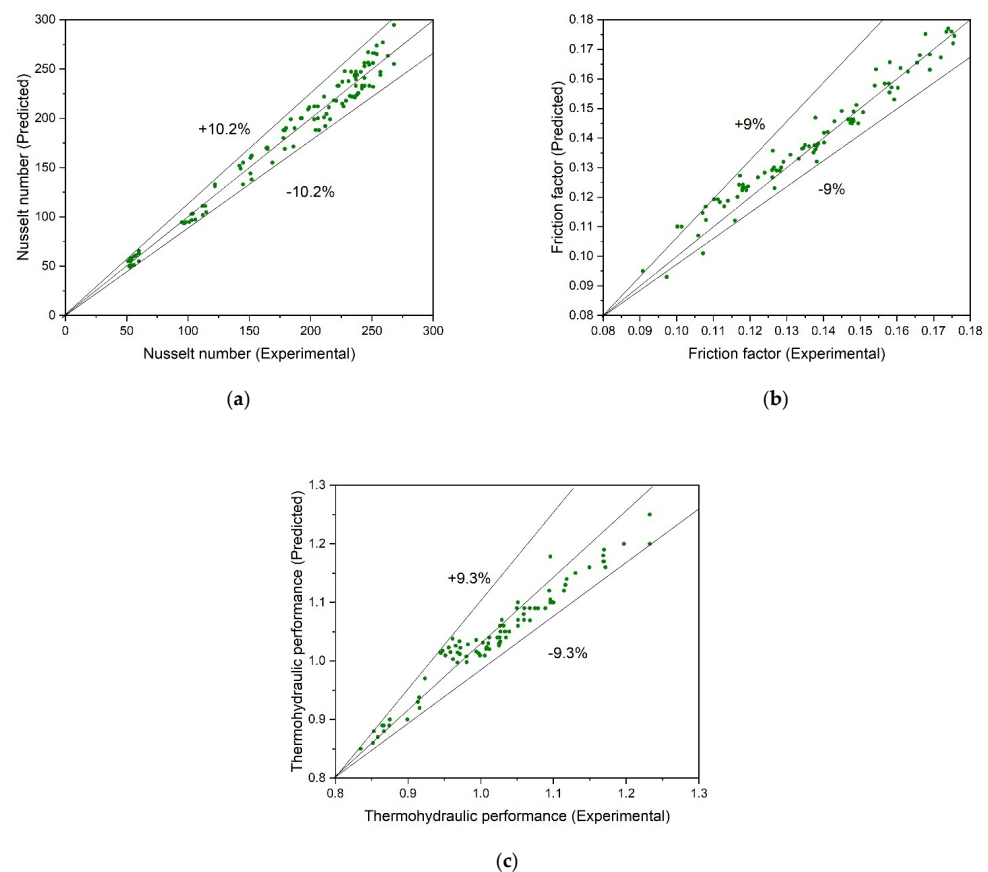
(a)

(b)

(c)

Figure 12. Deviation of experimental and predicted values of (**a**) Nu_{TT}, (**b**) f_{TT} and (**c**) η_{TT}.

10. Conclusions

In this paper, the effect of the nanoparticle concentration, dimpled rib height, dimpled rib pitch, and dimpled arc angle on the hydrothermal characteristics of $Al_2O_3 - H_2O$ nanofluid flow in a square duct are investigated experimentally. The key conclusions are presented here:

- Dimpled arc rib pitch, dimpled arc rib height, dimpled arc angle and volume fraction of nanofluid strongly affected the flow pattern and augmented the thermal-hydraulic performance of the square duct.
- In general, the Nu_{rs} and f_{rs} all tend to upsurge with the upsurge in nanoparticle concentration, attaining the highest value of nanoparticle concentration of 4.5% gives the highest values of both the Nu_{rs} and f_{rs} for the range of parameters investigated.
- A ratio of dimpled arc rib height to print diameter of 0.933 gives the highest value of Nu_{rs} and η_{per}, whereas a ratio of dimpled arc rib height to print diameter of 1.133 gives the highest value of the f_{rs}.
- A relative dimpled arc rib height of 4.64 gives the highest value of both the Nu_{rs} and η_{per}, whereas a relative dimpled arc rib height of 3.71 gives the highest value of the f_{rs}.
- In general, the value of Nu_{rs}, f_{rs} and η_{per} have been found to increase with increases in the values of dimpled arc angle. Attaining the maximum value of dimpled arc angle of $55°$ gives the highest values of Nu_{rs}, f_{rs} and η_{per} given the set of parameters examined.
- The maximum value of the thermal-hydraulic performance parameter occurs at φ_{np} of 4.5%, d_{np} of 30 nm, H_{AD}/P_d of 0.933, P_{AD}/H_{AD} of 4.64 and α_{AD} of $55°$ for Re_{num} of 11,000. The thermal-hydraulic performance characteristics' maximum value was discovered to be 1.23 for $Al_2O_3 - H_2O$-based nanofluid flow in a dimpled rib with arc pattern square duct for the range of parameters investigated.

Author Contributions: Conceptualization, A.K., R.M., S.S. and S.K.; methodology, M.S. and T.A. software, R.M., S.S. and S.K.; validation, T.A., A.K., S.M.E. and M.S.; formal analysis A.K., R.M., S.S. and T.A.; investigation, S.S. and S.K.; resources, M.S., N.K.G., S.M.E. and T.A.; data curation, A.K., R.M. and N.K.G.; writing—original draft preparation, A.K., R.M., S.M.E. and S.S.; writing—review and editing, A.K. and T.A.; visualization, A.K., R.M., S.S., S.M.E. and S.K.; supervision, M.S.; project administration, M.S. All authors have read and agreed to the published version of the manuscript.

Institutional Review Board Statement: Not applicable.

Informed Consent Statement: Not applicable.

Data Availability Statement: Data available on request.

Conflicts of Interest: The authors declare no conflict of interest.

Nomenclature

$C_{p, nf}$	Specific heat
d_{np}	Nanoparticle diameter
D_h	Hydraulic diameter
h	Convective heat transfer coefficient
H_{AD}	dimpled-arc-rib-height
P_{AD}	dimpled-rib-pitch
P_d	print diameter
Pr_{num}	Prandtl number
Nu_{rs}	Nusselt number of rough surface
f_{rs}	Friction factor of rough surface
k	Thermal conductivity
Greek symbols	
L	Duct length
$\dot{m}$	Mass flow rate

Re_{num}	Reynolds number
ΔP_d	Pressure drop across the duct
u_m	Fluid velocity
α_{AD}	dimpled arc angle
ϕ_{np}	Volume fraction
η_{rs}	Thermohydraulic performance parameter
ρ_{nf}	Nanofluid density
μ	Dynamic viscosity

References

1. Kumar, S.; Shandilya, M.; Chauhan, A.; Maithani, R.; Kumar, A. Experimental Analysis of Zinc Oxide/Water/Ethylene Glycol-Based Nanofluid in a Square Duct Roughened with Inclined Ribs. *J. Enhanc. Heat Transf.* **2020**, *27*, 687–709. [CrossRef]
2. Godson, L.; Raja, B.; Lal, D.M.; Wongwises, S. Enhancement of heat transfer using nanofluids—An overview. *Renew. Sustain. Energy Rev.* **2010**, *14*, 629–641. [CrossRef]
3. Babu, M.J.; Sandeep, N.; Saleem, S. Free convective MHD Cattaneo-Christov flow over three different geometries with thermophoresis and Brownian motion. *Alex. Eng. J.* **2017**, *56*, 659–669. [CrossRef]
4. Pandey, A.K.; Reji Kumar, R.; Kalidasan, B.; Laghari, I.A.; Samykano, M.; Kothari, R.; Abusorrah, A.M.; Sharma, K.; Tyagi, V.V. Utilization of solar energy for wastewater treatment: Challenges and progressive research trends. *J. Environ. Manag.* **2021**, *297*, 113300. [CrossRef]
5. Kumar, N.; Gupta, S.K.; Sharma, V.K. Application of phase change material for thermal energy storage: An overview of recent advances. *Mater. Today Proc.* **2021**, *44*, 368–375. [CrossRef]
6. Ogungbemi, A.T.; Adun, H.; Adedeji, M.; Kavaz, D.; Dagbasi, M. Does Particle Size in Nanofluid Synthesis Affect Their Performance as Heat Transfer Fluid in Flat Plate Collectors?—An Energy and Exergy Analysis. *Sustainability* **2022**, *14*, 10429. [CrossRef]
7. Arıkan, E.; Abbasoğlu, S.; Gazi, M. Experimental Performance Analysis of Flat Plate Solar Collectors Using Different Nanofluids. *Sustainability* **2018**, *10*, 1794. [CrossRef]
8. Kazem, H.A.; Chaichan, M.T.; Al-Waeli, A.H.A.; Jarimi, H.; Ibrahim, A.; Sopian, K. Effect of Temperature on the Electrical and Thermal Behaviour of a Photovoltaic/Thermal System Cooled Using SiC Nanofluid: An Experimental and Comparison Study. *Sustainability* **2022**, *14*, 11897. [CrossRef]
9. Giwa, S.O.; Sharifpur, M.; Ahmadi, M.H.; Meyer, J.P. Magnetohydrodynamic convection behaviours of nanofluids in non-square enclosures: A comprehensive review. *Math. Methods Appl. Sci.* **2020**, 1–59. [CrossRef]
10. Naseema; NawazishMehdia, S.; Hussain, M.M.; Basha, S.K.; Samad, M.A. Heat Enhancement of Heat Exchanger Using Aluminium Oxide(Al_2O_3), Copper Oxide(CuO)Nano Fluids with Different Concentrations. *Mater. Today Proc.* **2018**, *5 Pt 1*, 6481–6488. [CrossRef]
11. Karthikeyan, A.; Coulombe, S.; Kietzig, A. Boiling heat transfer enhancement with stable nanofluids and laser textured copper surfaces. *Int. J. Heat Mass Transf.* **2018**, *126*, 287–296. [CrossRef]
12. Dormohammadi, R.; Farzaneh-Gord, M.; Ebrahimi-Moghadam, A.; Ahmadi, M.H. Heat transfer and entropy generation of the nanofluid flow inside sinusoidal wavy channels. *J. Mol. Liq.* **2018**, *269*, 229–240. [CrossRef]
13. Shehzad, N.; Zeeshan, A.; Ellahi, R.; Vafai, K. Convective heat transfer of nanofluid in a wavy channel: Buongiorno's mathematical model. *J. Mol. Liq.* **2016**, *222*, 446–455. [CrossRef]
14. Tang, W.; Hatami, M.; Zhou, J.; Jing, D. Natural convection heat transfer in a nanofluid-filled cavity with double sinusoidal wavy walls of various phase deviations. *Int. J. Heat Mass Transf.* **2017**, *115*, 430–440. [CrossRef]
15. Sharifpur, M.; Solomon, A.B.; Ottermann, T.L.; Meyer, J.P. Optimum concentration of nanofluids for heat transfer enhancement under cavity flow natural convection with TiO_2—Water. *Int. Commun. Heat Mass Transf.* **2018**, *98*, 297–303. [CrossRef]
16. Solomon, A.B.; Sharifpur, M.; Ottermann, T.; Grobler, C.; Joubert, M.; Meyer, J.P. Natural convection enhancement in a porous cavity with Al_2O_3-Ethylene glycol/water nanofluids. *Int. J. Heat Mass Transf.* **2017**, *108*, 1324–1334. [CrossRef]
17. Garbadeen, I.; Sharifpur, M.; Slabber, J.; Meyer, J. Experimental study on natural convection of MWCNT-water nanofluids in a square enclosure. *Int. Commun. Heat Mass Transf.* **2017**, *88*, 1–8. [CrossRef]
18. Ghodsinezhad, H.; Sharifpur, M.; Meyer, J.P. Experimental investigation on cavity flow natural convection of Al_2O_3–Water nanofluids. *Int. Commun. Heat Mass Transf.* **2016**, *76*, 316–324. [CrossRef]
19. Joubert, J.; Sharifpur, M.; Solomon, A.B.; Meyer, J. Enhancement in heat transfer of a ferrofluid in a differentially heated square cavity through the use of permanent magnets. *J. Magn. Magn. Mater.* **2017**, *443*, 149–158. [CrossRef]
20. Mansoury, D.; Doshmanziari, F.I.; Kiani, A.; Chamkha, A.J. Heat transfer and flow characteristics of Al_2O_3/water nanofluid in various heat exchangers: Experiments on counter flow. *Heat Transf. Eng.* **2020**, *41*, 1–37. [CrossRef]
21. Mayeli, P.; Hesami, H.; Besharati-Foumani, H.; Niajalili, M. Al_2O_3–Water nanofluid heat transfer and entropy generation in a ribbed channel with wavy wall in the presence of magnetic field. *Numer. Heat Transf. Part A Appl.* **2018**, *73*, 604–623. [CrossRef]
22. Chun, B.-H.; Kang, H.U.; Kim, S.H. Effect of alumina nanoparticles in the fluid on heat transfer in double-pipe heat exchanger system. *Korean J. Chem. Eng.* **2008**, *25*, 966–971. [CrossRef]

23. Ghosh, S.; Mukhopadhyay, S. Flow and heat transfer of nanofluid over an exponentially shrinking porous sheet with heat and mass fluxes. *Propuls. Power Res.* **2018**, *7*, 268–275. [CrossRef]

24. Yang, C.; Wu, X.; Zheng, Y.; Qiu, T. Heat transfer performance assessment of hybrid nanofluids in a parallel channel under identical pumping power. *Chem. Eng. Sci.* **2017**, *168*, 67–77. [CrossRef]

25. Khoshvaght-Aliabadi, M.; Hormozi, F. Investigation on Heat Transfer and Pressure Drop of Copper–Water Nanofluid Flow in Plain and Perforated Channels. *Exp. Heat Transf.* **2015**, *29*, 427–444. [CrossRef]

26. Xuan, Y.; Li, Q. Investigation on Convective Heat Transfer and Flow Features of Nanofluids. *J. Heat Transf.* **2003**, *125*, 151–155. [CrossRef]

27. Xia, G.; Liu, R.; Wang, J.; Du, M. The characteristics of convective heat transfer in microchannel heat sinks using Al_2O_3 and TiO_2 nanofluids. *Int. Commun. Heat Mass Transf.* **2016**, *76*, 256–264. [CrossRef]

28. Parashar, A.K.; Gupta, A. Investigation of the effect of bagasse ash, hooked steel fibers and glass fibers on the mechanical properties of concrete. *Mater. Today Proc.* **2001**, *44*, 801–807. [CrossRef]

29. Ekiciler, R.; Çetinkaya, M.S.A. A comparative heat transfer study between monotype and hybrid nanofluid in a duct with various shapes of ribs. *Therm. Sci. Eng. Prog.* **2021**, *23*, 100913. [CrossRef]

30. Wang, G.; Feng, L.; Altanji, M.; Sharma, K.; Nisar, K.S.; Khorasani, S. Proposing novel "L" shaped fin to boost the melting performance of a vertical PCM enclosure. *Case Stud. Therm. Eng.* **2021**, *28*, 101465. [CrossRef]

31. Çobanoğlu, N.; Banisharif, A.; Estellé, P.; Karadeniz, Z.H. The developing flow characteristics of water—Ethylene glycol mixture based Fe_3O_4 nanofluids in eccentric annular ducts in low temperature applications. *Int. J. Thermofluids* **2022**, *14*, 100149. [CrossRef]

32. Vinoth, R.; Sachuthananthan, B.; Vadivel, A.; Balakrishnan, S.; Raj, A.G.S. Heat transfer enhancement in oblique finned curved microchannel using hybrid nanofluid. *Int. J. Therm. Sci.* **2023**, *183*, 107848. [CrossRef]

33. Fujimoto, K.; Shibata, A.; Torii, S. An experimental and numerical study of turbulent heat transfer enhancement for graphene nanofluids produced by pulsed discharge. *Int. J. Thermofluids* **2022**, *16*, 100219. [CrossRef]

34. Ho, C.; Huang, S.; Lai, C.-M. Enhancing laminar forced convection heat transfer by using Al_2O_3/PCM nanofluids in a concentric double-tube duct. *Case Stud. Therm. Eng.* **2022**, *35*, 102147. [CrossRef]

35. Jalili, B.; Aghaee, N.; Jalili, P.; Ganji, D.D. Novel usage of the curved rectangular fin on the heat transfer of a double-pipe heat exchanger with a nanofluid. *Case Stud. Therm. Eng.* **2022**, *35*, 102086. [CrossRef]

36. Zhang, H.; Nunayon, S.S.; Jin, X.; Lai, A.C. Pressure drop and nanoparticle deposition characteristics for multiple twisted tape inserts with partitions in turbulent duct flows. *Int. J. Heat Mass Transf.* **2022**, *193*, 121474. [CrossRef]

37. Omri, M.; Smaoui, H.; Frechette, L.; Kolsi, L. A new microchannel heat exchanger configuration using CNT-nanofluid and allowing uniform temperature on the active wall. *Case Stud. Therm. Eng.* **2022**, *32*, 101866. [CrossRef]

38. American Society of Heating, Refrigerating and Air-Conditioning Engineers. *Methods of Testing to Determine the Thermal Performance of Solar Collectors*; Technical Report ASHRAE-93-1986/XAB; ASHRAE: Washington, DC, USA, 1991.

39. Ho, C.; Wei, L.; Li, Z. An experimental investigation of forced convective cooling performance of a microchannel heat sink with Al_2O_3/water nanofluid. *Appl. Therm. Eng.* **2010**, *30*, 96–103. [CrossRef]

40. Vajjha, R.S.; Das, D.K. Experimental determination of thermal conductivity of three nanofluids and development of new correlations. *Int. J. Heat Mass Transf.* **2009**, *52*, 4675–4682. [CrossRef]

41. Seyf, H.R.; Mohammadian, S.K. Thermal and Hydraulic Performance of Counterflow Microchannel Heat Exchangers with and without Nanofluids. *J. Heat Transf.* **2011**, *133*, 081801. [CrossRef]

42. Vanaki, S.; Mohammed, H.; Abdollahi, A.; Wahid, M. Effect of nanoparticle shapes on the heat transfer enhancement in a wavy channel with different phase shifts. *J. Mol. Liq.* **2014**, *196*, 32–42. [CrossRef]

43. Dittus, F.W.; Boelter, L.M.K. Heat transfer in automobile radiators of the tubular type. *Int. Commun. Heat Mass Transf.* **1930**, *12*, 3–22. [CrossRef]

44. Sharma, S.; Das, R.K.; Kulkarni, K. Computational and experimental assessment of solar air heater roughened with six different baffles. *Case Stud. Therm. Eng.* **2021**, *27*, 101350. [CrossRef]

45. Klein, S. Calculation of flat-plate collector loss coefficients. *Sol. Energy* **1975**, *17*, 79–80. [CrossRef]

46. Webb, R.; Eckert, E. Application of rough surfaces to heat exchanger design. *Int. J. Heat Mass Transf.* **1972**, *15*, 1647–1658. [CrossRef]